SUPPLEMENTAL MATERIAL

Supplemental Methods

All procedures were carried out in accordance with the UK Animals Scientific Procedures Act (1986). Male Wistar rats (weight 200 g; Charles River, UK) were arbitrarily assigned to either a control or monocrotaline group. On day 0 the monocrotaline group received monocrotaline (Sigma-Aldrich Ltd, UK) 60 mg/kg by intraperitoneal injection and the control group received a volume matched 0.9% saline intraperitoneal injection (3 ml/kg). Monocrotaline was dissolved in 1 M hydrochloric acid and then made up to a concentration of 20 mg/ml with 0.9% saline, the pH corrected to 7.4 using 4 M NaOH. The animals were weighed and their clinical condition was assessed twice weekly in the first 18 days, and daily thereafter. The control and monocrotaline-injected animals were paired. Animals were sacrificed on the day that the following pre-specified endpoints were met, namely evidence of clinical deterioration with reduced movement, increased respiratory rate, piloerection and weight loss of >10 g over two days. The paired animal was sacrificed within 24 h. Animals that did not meet these criteria were electively sacrificed on day 28. The animals were sacrificed by stunning and cervical dislocation; the heart and lungs were excised and weighed.

In vivo ECG and echocardiography

Echocardiography and ECG recording was carried out under general anaesthesia with 2% isoflurane. Echocardiography images were acquired on an ACUSON Sequoia (Acuson Universal Diagnostics Solution, USA) with a 15 MHz 15L8 transducer. All images were stored on optical media disks for subsequent offline analysis. M-mode recordings were taken in the parasternal short axis view allowing recording of left ventricle anterior and posterior wall thickness and the internal diameter of the left ventricle in both systole and diastole. Right ventricle wall thickness was measured from M-mode recordings in the parasternal long axis view. Continuous wave Doppler recordings through the pulmonary artery were used to assess the pulmonary velocity profile. The maximum pulmonary velocity, time from the onset of pulmonary outflow to maximal flow (PAAT) and the rate of deceleration of pulmonary flow (PAD) were measured. ECG electrodes were inserted subcutaneously with the negative electrode in the right forepaw, the positive electrode in the left forepaw and the ground electrode in the right hindpaw. The electrodes were connected to a Bioamp and Powerlab analog to digital converter (AD Instruments, New Zealand). Signals were recorded using LabChart (AD Instruments, New Zealand) and analysed offline. Echocardiography and ECG recording was carried out on day 0 immediately prior to injection, day 21 and immediately prior to termination.

Telemetry

Telemetric recordings of ECGs from conscious and unrestrained male Wistar rats were made as part of an on-going study at the University of Leeds with UK Home Office and local ethical approval. For data included in this publication, animal source, monocrotaline treatment and experimental end points were the same as those described above with the additional voluntary ingestion of 2 ml/day blackcurrant juice placebo in the ongoing study. Implantation of recording devices and ECG acquisition were as previously described by Benoist *et al.*[1] Data were analysed using Chart 7 software (AD Instruments, New Zealand). Twenty-one days after injection of monocrotaline, ECGs were recorded 24 h per day.

Langendorff experiments

The heart was mounted on a Langendorff column and retrogradely perfused with oxygenated Tyrode's solution at a temperature of 36.5˚C with a fixed flow rate of 0.11 ml/g/min. Tyrode's solution contained: NaCl, 120 mM; $CaCl_2$, 1.2 mM; KCl, 4 mM; $MgSO_4$, 1.3 mM; NaH_2PO_4, 1.2 mM; $NaHC0_3$, 25.2 mM; glucose, 5.8 or 11 mM. The solution was equilibrated with 95%O_2 and 5% CO_2. Widely spaced extracellular electrodes were placed on the right atrium and left ventricle. The electrodes were connected via a headstage (NL100AK, Digitimer, UK) to an amplifier (NL104A, Digitimer, UK). The signal was then filtered between 50-500 Hz (NL125/6, Digitimer, UK). The amplified and filtered signal was then converted to a digital signal using a data acquisition unit (Micro 1401, Cambridge Electronic Design, UK) and recorded and analysed using Spike 2 software (Cambridge Electronic Design, UK). The electrodes record a 'pseudo-ECG' from the Langendorff-perfused heart which is equivalent to the *in vivo* ECG. The recording from 19-20 min (i.e. immediately prior to stimulation) was exported and analysed using LabChart software. This allowed an averaged ECG of the last 100 beats before stimulation to be inspected. The RR, PR and QT intervals and the QRS duration were measured. Pacing protocols were performed to measure atrial and ventricular effective refractory periods, atrioventricular (AV) node effective and functional refractory periods (AVERP and AVFRP, respectively) and Wenckebach cycle length. The pacing protocol for AVERP and AVFRP involved pacing the atrium with a drive train of 8 beats with a 180 ms coupling interval with an extra-stimulus with a progressively shortening coupling interval until failure of conduction between the atrium and ventricles was seen. The pacing protocol for Wenckebach cycle length used burst pacing of the atrium for 30 s at a fixed cycle length with a sequentially shortening cycle length until Wenckebach conduction was seen between the atrium and the ventricle.

Isolated AV node experiments

The heart was excised from the thorax and retrogradely perfused with oxygenated Tyrode's solution chilled to 4°C. The heart underwent dissection in a dissection chamber whilst being constantly superfused with oxygenated Tyrode's solution. The AV node preparation was placed in a perfusion bath with recirculated Tyrode's solution at a flow rate of 50 ml/min and temperature of 36.5°C. Custom made bipolar electrodes with an interelectrode spacing of 0.2 mm were used to record signals in the atrium and at the His bundle. Signals were amplified and filtered as per the Langendorff experiments. The preparation was stimulated with pacing protocols to determine AVERP, AVFRP and Wenckebach cycle length. The pacing protocol for AVERP and AVFRP involved pacing the atrium with a drive train of 15 beats with a coupling interval of 150 or 200 ms with an extra-stimulus with a progressively shortening coupling interval until failure of conduction between the atrium and ventricles was seen. The pacing protocol for determination of the Wenckebach cycle length used burst pacing of the atrium for 30 s at a fixed cycle length with a sequentially shortening cycle length until Wenckebach conduction was seen between the atrium and the His bundle.

Intracellular action potential recordings

Isolated AV node preparations were stimulated at 5 Hz at the level of the sinus node using 2 ms, 2× threshold, constant voltage rectangular pulses. Intracellular action potentials were recorded using sharp microelectrodes (20 to 40 MΩ resistances) filled with 3 M KCl as described previously by Atkinson *et al.*[2] Briefly, data acquired at 0.005 ms intervals using WinEDR V3.3.6 software (Dr J. Dempster, University of Strathclyde, Glasgow, UK) were passed through a 10 kHz low-pass Bessel filter, amplified 10 times (Axon Instruments GeneClamp 500) and digitised (Axon Instruments Digidata 1440A) for storage on a computer for later analysis.

AV node microdissection and reverse transcription quantitative polymerase chain reaction (qPCR)

Hearts were excised and the AV node dissection was carried out in the same way as for the isolated AV node experiments. The AV node was sectioned at 50 μm in a cryostat. Sections 300 μm apart were immunolabelled for HCN4 and Cx43 and stained with Masson's trichrome (Fig. S1). The immunolabelling and staining allowed six regions in and around the AV node to be identified: atrial septal myocardium, transitional tissue, inferior nodal extension, compact node, penetrating bundle and ventricular septal myocardium. A haematoxylin and eosin stain was performed on the remaining tissues and the six different regions were identified using a Nikon SMZ800 dissecting microscope (Nikon, Japan) with x63 magnification and were dissected with a sharp needle (Fig. S1). mRNA was extracted using the MirVana kit (Life Technologies, USA) and was treated with TurboDNAse (Life Technologies) to remove any residual genomic DNA. The concentration of mRNA in each sample was measured using the Qubit system (Life Technologies) and the samples were diluted so that 16 ng of total mRNA were used for reverse transcription. SuperScript VILO Mastermix (Life Technologies) with random hexamers was used to reverse transcribe the samples to cDNA. Prior to quantification, the cDNA underwent a preamplification process (Life Technologies); see below. The cDNA was quantified using the TaqMan low density array card system (TLDA; Life Technologies) using predesigned primer sequences with a hydrolysis probe detection system. Data were analysed using a combination of ExpressionSuite (Life Techonolgies) and RealTime Statminer (Integromics, S.L., USA) software. Samples that had failed to amplify for all or most targets were omitted. Where individual targets had not amplified in a sample where the majority of targets had amplified well, the undetermined values were replaced with a C_t value of 40 to represent an assumed very low abundance of the target within that sample. Expression was normalised to the abundance of a pair of housekeeper genes, B2M and PKG1, selected from 16 potential housekeeper genes as the most stable.

Preamplification

Because the tissues making up the AV node are small, the amount of RNA could be small (16 ng; less than the recommended minimum of 30 ng for Taqman low-density array cards) and therefore a preamplification step was performed after the RNA had been reverse transcribed to produce cDNA.[3,4] Preamplification of the cDNA was carried out using PCR and the combination of the specific primer sets for the genes of interest. The process of preamplification has been shown to increase the sensitivity of qPCR in several tissues,[3,4] but has not previously been used with heart tissue. To validate preamplification, 25 atrial and ventricular samples were used: 6 atrial and 7 ventricular samples from control rats and 6 atrial and 6 ventricular samples from monocrotaline-injected rats. Atrial and ventricular samples were used because relatively large amounts of RNA were isolated. From the samples, two cDNA dilutions were prepared from each: one with an effective initial total RNA of 16 ng (which was preamplified) and another with an effective initial total RNA of 160 ng (which was not preamplified). qPCR using Taqman low-density array cards was then used to measure the expression of the 95 transcripts of interest in the samples using both dilutions. Expression was normalised to the abundance of the housekeeper genes, B2M and PKG1 (ΔC_t=C_t housekeeper–C_t target). If preamplification is effective, the ΔC_t value for a target transcript should be the same for the unamplified and preamplified samples. Fig. S2 shows the relationship between the ΔC_t values from the unamplified and preamplified samples for all transcripts and all tissue samples. The ΔC_t values for the unamplified and preamplified samples are significantly correlated ($P<0.0001$) with an R^2 value of 0.61. The correlation is excellent for abundantly expressed transcripts ($\Delta C_t<0$; transcript of interest more abundant than housekeeper). However, there is deviation from a 1:1 relationship for poorly expressed transcripts ($\Delta C_t>0$; transcript of interest less abundant than housekeeper). It is likely that low concentrations of cDNA for targets in the unamplified samples were at the limit of detection of qPCR and therefore inaccurate quantification of these targets in the unamplified samples caused deviation from the 1:1 relationship. These findings support the validity of the preamplification methodology and show the need for preamplification with the low concentrations of mRNA in the microdissected tissue samples from the AV node.

Immunohistochemistry

Whole hearts were cryosectioned, the different regions of the cardiac conduction system including the AV node identified by histology and neurofilament 150 and HCN4 immunolabelled as described previously.[5-7]

Computer modelling

mRNA is an important determinant of protein (and therefore function), although not the only determinant (it can account for ~40% of variation[8-10]). In the cardiac conduction system, we have usually (but not always) seen a correlation between mRNA and protein.[e.g.11] We and others have successfully used biophysically-detailed action potential models to predict potential changes in electrical activity based on changes in mRNA expression for ion channels etc.[11-16] We scale the conductance for a particular ionic current based on the change in the corresponding mRNA. This is not a method of generating definitive biophysically-detailed action potential models, but instead is a form of bioinformatics to explore the *possible* consequences of changes in transcripts and we have used this approach in the present study. A one-dimensional (1D) strand model of cardiac tissue was constructed in order to simulate the functional effects of pulmonary hypertension (PHT) on action potential conduction. The 1D model is 52.5 mm in length and consists of segments of atrium (15 mm), AV node (12.5 mm), Purkinje fibre (20 mm) and ventricle (10 mm). The segments were simulated by well-established models of the action potential of an atrial cell,[17] AV node cells,[18] Purkinje cell and left ventricular cell[19] of the rabbit heart (action potential models are not available for other species). Details of the dimensions and coupling conductances of the 1D strand model are summarised in Table S4. For simplicity, we chose to only consider the fast pathway (the normal pathway) through the AV node. For initiation of cardiac excitation, a series of supra-threshold stimuli were applied at the beginning of the strand of atrium; each stimulus evoked an action potential that propagated from the atrium to the AV node, and then to the Purkinje fibres and ventricular muscle. The PHT condition was simulated based on regional changes in mRNA expression, which we assumed to reflect changes in the corresponding ion channel current density as we and others have done previously.[11-16] The ratio of an ionic conductance in PHT to the same ionic conductance in control, g'_{ion}, was calculated as follows:

$$g'_{ion} = \frac{\left(\sum_{i=1}^{n} \gamma_{ion}^{i} d_{ion}^{i}\right)_{PHT}}{\left(\sum_{i=1}^{n} \gamma_{ion}^{i} d_{ion}^{i}\right)_{control}},$$

where γ_{ion} is the single channel conductance (values used listed in Table S5) and d_{ion} is the density (or expression) of the relevant ion channel. In many cases, more than one ion channel contributes to an ionic conductance and the ionic conductance was calculated by summing the contribution of the different ion channels. Details of the calculations are shown in Tables S6-S10. The changes made to simulate PHT are summarised in Table S11. The 1D cable equation was solved using the Forward-Time Central-Space scheme with a space step of 0.1 mm and time step of 0.005 ms.

Supplemental Discussion

Validation of the monocrotaline model

There are several animal models of PHT and the monocrotaline model is the best characterised and most widely used.[20,21] Monocrotaline is a pyrrolizidine alkaloid, extracted from the plant *Crotalaria spectabilis*, and a single injection has been shown to generate severe pulmonary arterial hypertension in several species, notably the rat.[e.g.22,23] Experiments using the monocrotaline model have given positive results from drug therapies including ERAs, sildenafil, statins and β-blockers that have gone on to become the mainstay of therapy for patients with pulmonary arterial hypertension.[24-28] The monocrotaline model has been used to investigate arrhythmias in the working myocardium.[1,16,29] Although the monocrotaline model is widely used there remain some concerns over its representativeness as a model of PHT.[30] Histological examination of the lungs of monocrotaline-injected rats shows medial thickening and muscular hypertrophy, but not the characteristic plexiform lesions that are seen in patients with PHT.[30] There is also concern regarding the possibility that monocrotaline may have a direct effect on the heart and therefore any changes seen in cardiac function may be attributable to a direct effect of monocrotaline and not PHT. One study demonstrated inflammation in the right ventricular free wall, interventricular septum and posterior left ventricular wall in response to monocrotaline injection with some evidence of inflammation in the posterior left ventricle wall prior to the development of PHT. The authors argue that this demonstrates a direct toxic effect of monocrotaline on the heart.[31] In contrast to this, another study using both *in vivo* single-photon emission computed tomography imaging and *ex vivo* histological and PCR techniques demonstrated that inflammation was largely confined to the right ventricle and interventricular septum. The authors argue that inflammation is part of the pathogenesis of right heart failure secondary to PHT rather than a direct monocrotaline effect.[32] Support for this view comes from the finding of right ventricular inflammation in a rat model of pulmonary embolism and PHT.[33] The conflicting findings regarding left ventricular involvement in the monocrotaline model may in part be explained by which areas of the left ventricle were studied; the study reporting inflammation in the left ventricle looked at the posterior wall which is in close proximity to the septum and posterior attachment of the right ventricle.[31] There are several arguments that support the use of the monocrotaline model to investigate the effects of PHT. The success of several pharmacological therapies showing beneficial effects on respiratory physiology and cardiac function in both the monocrotaline model and in humans would not be expected if the deleterious effects on cardiac function seen in the monocrotaline model were purely due to a direct toxic effect of monocrotaline.[24-26,34] In our study, we are interested in the effects of PHT on the heart and therefore concerns regarding the lack of plexiform lesions in the monocrotaline model are less relevant given the known increases in right heart pressures with the monocrotaline model. The monocrotaline model is technically simple (with a single subcutaneous injection developing a severe PHT phenotype in 3-4 weeks), well characterised and has previously been used to investigate arrhythmias in the working myocardium.

Site of conduction block

The experimental data in Fig. 3 and Table S1 shows that heart block most often occurs in the compact node in PHT. However, whereas many significant changes in ion channel expression were observed in the inferior nodal extension, fewer were observed in the compact node (Table S3). However, the same trend of downregulation of L-type Ca^{2+} channels was observed in the compact node as in the inferior nodal extension (Fig. 4). The computer model, which was based on the measured changes in ion channel expression, predicted block in the compact node (Fig. 8). There is therefore a reasonable correlation between observation and prediction.

Limitations of the study

In vivo the AV node dysfunction was generally relatively modest (Table 1). As argued above, in part this is because AV node function may be supported *in vivo* by an increase in sympathetic tone. However, in addition, the animal legislation in the UK does not permit animals reaching end stage heart failure. In this study, gene expression has been measured at the mRNA level. Determination of protein expression is difficult. For example, many ion channel antibodies are poor and the specialised tissues of the heart of small mammals are too small for Western blot. However, in a pilot experiment we confirmed that there is a downregulation of HCN4 protein in the AV node in PHT (Fig. S8) consistent with the downregulation of HCN4 mRNA (Fig. 4).

Supplemental References

1. Benoist D, Stones R, Drinkhill MJ, Benson AP, Yang Z, Cassan C, Gilbert SH, Saint DA, Cazorla O, Steele DS, Bernus O and White E. Cardiac arrhythmia mechanisms in rats with heart failure induced by pulmonary hypertension. *American Journal of Physiology - Heart and Circulatory Physiology*. 2012;302:H2381-95.
2. Atkinson AJ, Logantha SJ, Hao G, Yanni J, Fedorenko O, Sinha A, Gilbert SH, Benson AP, Buckley DL, Anderson RH, Boyett MR and Dobrzynski H. Functional, anatomical, and molecular investigation of the cardiac conduction system and arrhythmogenic atrioventricular ring tissue in the rat heart. *Journal of the American Heart Association*. 2013;2:e000246.
3. Demarest TG, Murugesan N, Shrestha B and Pachter JS. Rapid expression profiling of brain microvascular endothelial cells by immuno-laser capture microdissection coupled to TaqMan low density array. *Journal of Neuroscience Methods*. 2012;206:200-4.

4. Ishii S, Segawa T and Okabe S. Simultaneous quantification of multiple food- and waterborne pathogens by use of microfluidic quantitative PCR. *Applied and Environmental Microbiology*. 2013;79:2891-8.
5. Yanni J, Boyett MR, Anderson RH and Dobrzynski H. The extent of the specialized atrioventricular ring tissues. *Heart Rhythm*. 2009;6:672-680.
6. Yanni J, Tellez JO, Sutyagin PV, Boyett MR and Dobrzynski H. Structural remodelling of the sinoatrial node in obese old rats. *Journal of Molecular and Cellular Cardiology*. 2010;48:653-662.
7. Dobrzynski H, Li J, Tellez J, Greener ID, Nikolski VP, Wright SE, Parson SH, Jones SA, Lancaster MK, Yamamoto M, Honjo H, Takagishi Y, Kodama I, Efimov IR, Billeter R and Boyett MR. Computer three-dimensional reconstruction of the sinoatrial node. *Circulation*. 2005;111:846-854.
8. Tian Q, Stepaniants SB, Mao M, Weng L, Feetham MC, Doyle MJ, Yi EC, Dai H, Thorsson V, Eng J, Goodlett D, Berger JP, Gunter B, Linseley PS, Stoughton RB, Aebersold R, Collins SJ, Hanlon WA and Hood LE. Integrated genomic and proteomic analyses of gene expression in Mammalian cells. *Molecular & Cellular Proteomics*. 2004;3:960-9.
9. Fu N, Drinnenberg I, Kelso J, Wu JR, Paabo S, Zeng R and Khaitovich P. Comparison of protein and mRNA expression evolution in humans and chimpanzees. *PLoS One*. 2007;2:e216.
10. Maier T, Guell M and Serrano L. Correlation of mRNA and protein in complex biological samples. *FEBS Letters*. 2009;583:3966-73.
11. Chandler NJ, Greener ID, Tellez JO, Inada S, Musa H, Molenaar P, DiFrancesco D, Baruscotti M, Longhi R, Anderson RH, Billeter R, Sharma V, Sigg DC, Boyett MR and Dobrzynski H. Molecular architecture of the human sinus node - insights into the function of the cardiac pacemaker. *Circulation*. 2009;119:1562-1575.
12. Abd Allah ESH, Tellez JO, Aslanidi OV, Zhang H, Dobrzynski H and Boyett MR. Postnatal development of transmural gradients in expression of ion channels and Ca^{2+}-handling proteins in the ventricle. *Journal of Molecular and Cellular Cardiology*. 2012;53:145-155.
13. Dobrzynski H, Anderson RH, Atkinson A, Borbas Z, D'Souza A, Fraser JF, Inada S, Logantha SJRJ, Monfredi O, Morris GM, Moorman AFM, Nikolaidou T, Schneider H, Szuts V, Temple IP, Yanni J and Boyett MR. Structure, function and clinical relevance of the cardiac conduction system, including the atrioventricular ring and outflow tract tissues. *Pharmacology & Therapeutics*. 2013;139:260-288.
14. Hao XZ, Y.; Zhang, X.; Nirmalan, M.; Davies, L.; Dobrzynski, H.; Wang, X.; Grace, A.A.; Zhang, H., Boyett, M.R.; Huang, C.L.-H.; Lei, M. TGF-β1 mediated fibrosis and ion channel remodeling are key mechanisms producing sinus node dysfunction associated with SCN5A deficiency and aging. *Circulation: Arrhythmia and Electrophysiology*. 2011;4:397-406.
15. Li J, Logantha SJ, Yanni J, Cai X, Dobrzynski H, Hart G and Boyett M. Computer simulation of failing rabbit Purkinje fibres. *Computers in Cardiology*. 2013;40:361-364.
16. Benoist D, Stones R, Drinkhill M, Bernus O and White E. Arrhythmogenic substrate in hearts of rats with monocrotaline-induced pulmonary hypertension and right ventricular hypertrophy. *American Journal of Physiology*. 2011;300:H2230-H2237.
17. Aslanidi OV, Dewey RS, Morgan AR, Boyett MR and Zhang H. Regional differences in rabbit atrial action potential properties: mechanisms, consequences and pharmacological implications. *Conference Proceedings of IEEE Engineering in Medicine & Biology Society*. 2008;2008:141-144.
18. Inada S, Hancox JC, Zhang H and Boyett MR. One-dimensional mathematical model of the atrioventricular node including atrio-nodal, nodal, and nodal-his cells. *Biophysical Journal*. 2009;97:2117-2127.
19. Aslanidi OV, Sleiman RN, Boyett MR, Hancox JC and Zhang H. Ionic mechanisms for electrical heterogeneity between rabbit Purkinje fiber and ventricular cells. *Biophysical Journal*. 2010;98:2420-31.
20. Stenmark KR, Meyrick B, Galie N, Mooi WJ and McMurtry IF. Animal models of pulmonary arterial hypertension: the hope for etiological discovery and pharmacological cure. *American Journal of Physiology*. 2009;297:L1013-32.
21. Pak O, Janssen W, Ghofrani HA, Seeger W, Grimminger F, Schermuly RT and Weissmann N. Animal models of pulmonary hypertension: role in translational research. *Drug Discovery Today: Disease Models*. 2011;7:89-97.

22. Wilson DW, Segall HJ, Pan LC and Dunston SK. Progressive inflammatory and structural changes in the pulmonary vasculature of monocrotaline-treated rats. *Microvascular Research*. 1989;38:57-80.
23. Kay JM, Harris P and Heath D. Pulmonary hypertension produced in rats by ingestion of Crotalaria spectabilis seeds. *Thorax*. 1967;22:176-9.
24. Clozel M, Hess P, Rey M, Iglarz M, Binkert C and Qiu C. Bosentan, sildenafil, and their combination in the monocrotaline model of pulmonary hypertension in rats. *Experimental Biology and Medicine*. 2006;231:967-973.
25. Hamidi SA, Lin RZ, Szema AM, Lyubsky S, Jiang YP and Said SI. VIP and endothelin receptor antagonist: an effective combination against experimental pulmonary arterial hypertension. *Respiratory Research*. 2011;12:141.
26. Iglarz M, Binkert C, Morrison K, Fischli W, Gatfield J, Treiber A, Weller T, Bolli MH, Boss C, Buchmann S, Capeleto B, Hess P, Qiu C and Clozel M. Pharmacology of macitentan, an orally active tissue-targeting dual endothelin receptor antagonist. *Journal of Pharmacology and Experimental Therapeutics*. 2008;327:736-45.
27. McMurtry MS, Bonnet S, Michelakis ED, Bonnet S, Haromy A and Archer SL. Statin therapy, alone or with rapamycin, does not reverse monocrotaline pulmonary arterial hypertension: the rapamcyin-atorvastatin-simvastatin study. *American Journal of Physiology - Lung Cellular and Molecular Physiology*. 2007;293:L933-40.
28. Mouchaers KT, Schalij I, Versteilen AM, Hadi AM, van Nieuw Amerongen GP, van Hinsbergh VW, Postmus PE, van der Laarse WJ and Vonk-Noordegraaf A. Endothelin receptor blockade combined with phosphodiesterase-5 inhibition increases right ventricular mitochondrial capacity in pulmonary arterial hypertension. *American Journal of Physiology - Heart and Circulatory Physiology*. 2009;297:H200-7.
29. Uzzaman M, Honjo H, Takagishi Y, Emdad L, Magee AI, Severs NJ and Kodama I. Remodeling of gap junctional coupling in hypertrophied right ventricles of rats with monocrotaline-induced pulmonary hypertension. *Circulation Research*. 2000;86:871-878.
30. Stenmark KR, Meyrick B, Galie N, Mooi WJ and McMurtry IF. Animal models of pulmonary arterial hypertension: the hope for etiological discovery and pharmacological cure. *American Journal of Physiology - Lung Cellular and Molecular Physiology*. 2009;297:L1013-32.
31. Akhavein F, St-Michel EJ, Seifert E and Rohlicek CV. Decreased left ventricular function, myocarditis, and coronary arteriolar medial thickening following monocrotaline administration in adult rats. *Journal of Applied Physiology*. 2007;103:287-95.
32. Campian ME, Hardziyenka M, de Bruin K, van Eck-Smit BL, de Bakker JM, Verberne HJ and Tan HL. Early inflammatory response during the development of right ventricular heart failure in a rat model. *European Journal of Heart Failure*. 2010;12:653-8.
33. Watts JA, Zagorski J, Gellar MA, Stevinson BG and Kline JA. Cardiac inflammation contributes to right ventricular dysfunction following experimental pulmonary embolism in rats. *Journal of Molecular and Cellular Cardiology*. 2006;41:296-307.
34. Dupuis J and Prie S. The ET(A)-receptor antagonist LU 135252 prevents the progression of established pulmonary hypertension induced by monocrotaline in rats. *Journal of cardiovascular pharmacology and therapeutics*. 1999;4:33-39.
35. Brandt MC, Endres-Becker J, Zagidullin N, Motloch LJ, Er F, Rottlaender D, Michels G, Herzig S and Hoppe UC. Effects of KCNE2 on HCN isoforms: distinct modulation of membrane expression and single channel properties. *American Journal of Physiology - Heart and Circulatory Physiology*. 2009;297:H355-63.
36. Vanoye CG, Lossin C, Rhodes TH and George AL, Jr. Single-channel properties of human $Na_v1.1$ and mechanism of channel dysfunction in SCN1A-associated epilepsy. *Journal of General Physiology*. 2006;127:1-14.
37. Beyder A, Rae JL, Bernard C, Strege PR, Sachs F and Farrugia G. Mechanosensitivity of Nav1.5, a voltage-sensitive sodium channel. *Journal of Physiology*. 588:4969-85.
38. Navedo MF, Amberg GC, Westenbroek RE, Sinnegger-Brauns MJ, Catterall WA, Striessnig J and Santana LF. $Ca_v1.3$ channels produce persistent calcium sparklets, but $Ca_v1.2$ channels are responsible for sparklets in mouse arterial smooth muscle. *American Journal of Physiology - Heart and Circulatory Physiology*. 2007;293:H1359-70.
39. Bittner KC and Hanck DA. The relationship between single-channel and whole-cell conductance in the T-type Ca^{2+} channel $Ca_v3.1$. *Biophysical Journal*. 2008;95:931-41.

40. Zhu J, Watanabe I, Gomez B and Thornhill WB. Heteromeric Kv1 potassium channel expression: amino acid determinants involved in processing and trafficking to the cell surface. *Journal of Biological Chemistry*. 2003;278:25558-67.

41. Wang Z, Eldstrom JR, Jantzi J, Moore ED and Fedida D. Increased focal Kv4.2 channel expression at the plasma membrane is the result of actin depolymerization. *American Journal of Physiology - Heart and Circulatory Physiology*. 2004;286:H749-59.

42. Jerng HH, Qian Y and Pfaffinger PJ. Modulation of Kv4.2 channel expression and gating by dipeptidyl peptidase 10 (DPP10). *Biophysical Journal*. 2004;87:2380-96.

43. Liu GX, Derst C, Schlichthorl G, Heinen S, Seebohm G, Bruggemann A, Kummer W, Veh RW, Daut J and Preisig-Muller R. Comparison of cloned Kir2 channels with native inward rectifier K^+ channels from guinea-pig cardiomyocytes. *Journal of Physiology*. 2001;532:115-126.

44. Boyett MR, Inada S, Yoo S, Li J, Liu J, Tellez JO, Greener ID, Honjo H, Billeter R, Lei M, Zhang H, Efimov IR and Dobrzynski H. Connexins in the sinoatrial and atrioventricular nodes. *Advances in Cardiology*. 2006;42:175-197.

Table S1. Normal and abnormal electrical conduction through the isolated AV node from control and PHT rats.

Conduction phenotype	Incidence	
	Control	PHT
Normal 1:1 conduction through AV node	4/5	1/6
Conduction block in compact node (e.g. Fig. 3B)	1/5	3/6
Decremental conduction in penetrating bundle and likely complete block (Fig. 3C)	0/5	1/6
Decremental conduction in the penetrating bundle	0/5	1/6

Table S2. Expression of all transcripts. Expression of a transcript is given as a percentage of the expression of the same transcript in the control atrial sample. Significant differences (FDR<0.2) between the control and PHT groups are marked with arrows. A red highlighted arrow indicates significant downregulation in the PHT group and a green highlighted arrow indicates significant upregulation in the PHT group. MCT, monocrotaline.

	Atrium		**Transitional tissue**		**Inferior nodal extension**		**Compact node**		**Penetrating bundle**		**Ventricle**	
	Control	**MCT**	**Control**	**MCT**	**Control**	**MCT**	**Control**	**MCT**	**Control**	**MCT**	**Control**	**MCT**
Inward currents												
$\mathrm{Na_V}$1.1	100	61 ↓	90	40 ↓	49	16	67	33	20	23	53	78
$\mathrm{Na_V}$1.5	100	169	45	75	11	17	9	21	33	57	167	103
$\mathrm{Na_V}$1.8	100	47	16	18	9	88	4	40	687	347	3	7 ↑
$\mathrm{Na_V}\beta1$	100	111	70	91	27	44	43	46	22	32	112	121
$\mathrm{Ca_V}$1.2	100	46 ↓	146	84	93	48 ↓	80	36	90	54	62	101 ↑
$\mathrm{Ca_V}$1.3	100	16	17	0	45	0 ↓	36	16	52	3	16	7
$\mathrm{Ca_V}$3.1	100	38	41	8	39	9	45	46	30	5	14	10
$\mathrm{Ca_V}$3.2	100	45	14	1	22	2	27	12	18	19	43	34 ↓
$\mathrm{Ca_V}\alpha2\delta1$	100	77	21	15	18	5	9	8	7	15	71	45
$\mathrm{Ca_V}2\delta2$	100	83	18	3	31	4	48	79	111	9	58	30 ↓
$\mathrm{Ca_V}\beta2$	100	113	42	34	15	18	23	36	17	29	87	128
HCN1	100	147	234	213	426	239	426	372	143	235	1	7 ↑
HCN2	100	80	32	17	27	16	20	25	18	114	1299	385 ↓
HCN4	100	39 ↓	487	154	800	143 ↓	1162	343 ↓	2428	853	78	119
CLC-2	100	71	98	77	58	30	69	69	69	91	86	82
CLC-3	100	79	87	72	182	71 ↓	117	106	133	143	55	156 ↑

Table S2 (continued).

	Atrium		Transitional tissue		Inferior nodal extension		Compact node		Penetrating bundle		Ventricle	
	Control	MCT	Control	MCT	Control	MCT	Control	MCT	Control	MCT	Control	MCT
Outward currents												
Kv1.2	100	9 ↓	17	1	9	0 ↓	3	2	15	2	20	7
Kv1.4	100	36 ↓	35	11	8	3	12	10	9	7	25	26
Kv1.5	100	74	158	109	179	51 ↓	192	156	136	92	57	48
Kv2.1	100	56 ↓	65	38	33	20	35	30	28	30	143	84 ↓
Kv4.2	100	14 ↓	13	1	10	2 ↓	1	1	1	9	97	38 ↓
Kv4.3	100	49 ↓	61	39	45	22 ↓	38	25	31	14	37	15 ↓
ERG1	100	39 ↓	38	8	13	5	13	13	14	14	54	32 ↓
K$_V$LQT1	100	83	35	14	16	14	26	17	20	24	109	84
K$_{ir}$2.1	100	48 ↓	76	41	20	21	27	24	74	80	149	159
K$_{ir}$2.2	100	33	19	3	19	1	11	4	5	7	43	22 ↓
K$_{ir}$2.4	100	117	20	0	24	2 ↓	24	2	23	26	357	72 ↓
K$_{ir}$3.1	100	26 ↓	36	6 ↓	8	3	7	3	5	2	18	7 ↓
K$_{ir}$3.4	100	58 ↓	117	70	59	31 ↓	86	51	32	24	10	19 ↑
K$_{ir}$6.1	100	72 ↓	69	71	83	74	48	65	46	96	96	108
K$_{ir}$6.2	100	36 ↓	51	12 ↓	25	4	21	19	16	19	208	84 ↓
SUR1	100	60	24	9	11	4	10	10	3	15	120	41 ↓
SUR2	100	51 ↓	72	47	57	39	40	28	71	58	82	72
KChIP2	100	24 ↓	59	37 ↓	121	11 ↓	21	4 ↓	39	23	270	170 ↓
minK	100	1060	104	96	98	8 ↓	240	124	154	77	354	694
TWIK1	100	93	27	3	41	2 ↓	13	12	86	32	14	17
TASK1	100	70	37	26	15	7	10	18	9	24	90	54 ↓

Table S2 (continued).

	Atrium		Transitional tissue		Inferior nodal extension		Compact node		Penetrating bundle		Ventricle	
	Control	**MCT**	**Control**	**MCT**	**Control**	**MCT**	**Control**	**MCT**	**Control**	**MCT**	**Control**	**MCT**
Intracellular Ca^{2+} cycling												
RyR2	100	43 ↓	20	3	9	1 ↓	20	8	8	14	87	63
RyR3	100	85	49	54	14	16	18	21	9	21	42	48
NCX1	100	73	36	18	30	8	48	34	56	22	65	52
SERCA2a	100	56	69	38	46	19	35	31	12	13	30	81
Phospholamban	100	25 ↓	88	29 ↓	93	18 ↓	92	34 ↓	98	61	70	123
PMCA1	100	103	71	69	84	58	77	68	80	82	91	69
Calsequestrin 2	100	87	55	39	29	20	48	38	25	20	83	65
Sarcolipin	100	28 ↓	89	31 ↓	56	16 ↓	38	16	2	1	0	0
Connexins												
Cx30.2	100	47	1743	1 ↓	3249	20 ↓	3012	1415	1374	65	55	35
Cx43	100	50	17	14	5	2	3	4	2	18	86	56
Cx40	100	170	41	40	43	25	35	36	622	337	188	287
Cx45	100	99	125	113	127	104	158	132	311	247	55	111↑
Ion channel transporters												
Na^+/K^+ ATPase α1 subunit	100	71	114	94	66	60	107	85	82	93	34	51↑
Na^+/K^+ ATPase α2 subunit	100	40 ↓	90	56	103	37 ↓	81	54	113	82	174	102 ↓
Na^+/K^+ ATPase α3 subunit	100	129	184	99	896	97 ↓	1078	283 ↓	405	97	210	34 ↓
Na^+/K^+ ATPase β1 subunit	100	146	30	56	16	25	22	41	21	18	68	44 ↓
Na^+/H^+ transporter	100	88	76	72	45	69 ↑	104	81	78	65	53	54

Table S2 (continued).

	Atrium		Transitional tissue		Inferior nodal extension		Compact node		Penetrating bundle		Ventricle	
	Control	**MCT**	**Control**	**MCT**	**Control**	**MCT**	**Control**	**MCT**	**Control**	**MCT**	**Control**	**MCT**
Autonomic regulators												
α1a/1c adrenergic receptor,	100	58 ↓	34	22	29	8 ↓	33	27	27	48	121	119
α1b adrenergic receptor,	100	34	23	0	24	0	22	14	17	52	370	144 ↓
β1 adrenergic receptor	100	62	103	82	88	46 ↓	85	77	68	42	80	61
β2 adrenergic receptor	100	58 ↓	121	81	99	75	95	93	63	95	81	85
M2 muscarinic receptor	100	48 ↓	23	12	14	4	13	18	5	9	25	30
A1 adenosine receptor	100	116	21	20	36	12	16	59	8	15	40	34

Table S3. Summary of transcripts significantly (FDR<0.2) altered in the different regions of the AV node in PHT. Red downward arrow, downregulation in PHT; green upward arrow, upregulation. *P* value from limma test and FDR-corrected *P* value given.

Atrial muscle	P value	Adjusted P value	Transitional tissue	P value	Adjusted P value	Inferior nodal extension	P value	Adjusted P value
HCN4 ↓	<0.01	0.03	Na$_v$1.1 ↓	0.01	0.10	HCN4 ↓	<0.01	<0.01
Na$_v$1.1 ↓	0.05	0.17	KChIP2 ↓	0.02	0.14	Ca$_v$1.2 ↓	0.06	0.18
Ca$_v$1.2 ↓	0.01	0.04	K$_{ir}$3.1 ↓	0.01	0.10	Ca$_v$1.3 ↓	<0.01	<0.01
K$_v$1.4 ↓	<0.01	0.04	K$_{ir}$6.2 ↓	<0.01	0.06	CLC-3 ↓	0.06	0.18
K$_v$4.2 ↓	0.02	0.07	Phospholamban ↓	<0.01	0.03	K$_v$4.2 ↓	0.06	0.19
K$_v$4.3 ↓	0.01	0.04	Sarcolipin ↓	<0.01	0.04	K$_v$4.3 ↓	0.05	0.18
KChIP2 ↓	<0.01	0.02	Cx30.2 ↓	0.01	0.10	KChIP2 ↓	<0.01	<0.01
K$_v$1.2 ↓	<0.01	0.04				K$_v$1.2 ↓	0.04	0.17
K$_v$2.1 ↓	0.05	0.17				K$_v$1.5 ↓	<0.01	<0.01
ERG1 ↓	0.06	0.17				minK ↓	0.02	0.10
K$_{ir}$2.1 ↓	0.01	0.04				K$_{ir}$2.4 ↓	0.01	0.04
K$_{ir}$3.1 ↓	0.01	0.04				K$_{ir}$3.4 ↓	0.01	0.08
K$_{ir}$3.4 ↓	0.04	0.14				TWIK1 ↓	<0.01	<0.01
K$_{ir}$6.1 ↓	0.06	0.19				RyR2 ↓	<0.01	0.02
K$_{ir}$6.2 ↓	0.01	0.04				Phospholamban ↓	<0.01	<0.01
SUR2 ↓	0.01	0.04				Sarcolipin ↓	<0.01	0.02
RyR2 ↓	0.02	0.07				Cx30.2 ↓	<0.01	<0.01
Phospholamban ↓	<0.01	0.01				Na$^+$/K$^+$ ATPase α2 subunit ↓	<0.01	0.02
Sarcolipin ↓	<0.01	0.01				Na$^+$/K$^+$ ATPase α3 subunit ↓	<0.01	<0.01
Na$^+$/K$^+$ ATPase α2 subunit ↓	<0.01	0.03				Na$^+$/H$^+$ transporter ↑	0.07	0.20
M2 muscarinic receptor ↓	0.05	0.17				1a/1c adrenergic receptor ↓	0.02	0.09
1a/1c adrenergic receptor ↓	0.03	0.11				β1 adrenergic receptor ↓	0.06	0.18
β2 adrenergic receptor ↓	0.01	0.05						

Table S3 (continued).

Compact node	P value	Adjusted P value	Ventricular muscle	P value	Adjusted P value
HCN4 ↓	<0.01	0.03	HCN1 ↑	0.02	0.16
KChIP2 ↓	<0.01	0.03	HCN2 ↓	0.01	0.04
Phospholamban ↓	0.01	0.08	Na$_v$1.8 ↑	0.02	0.08
Na$^+$/K$^+$ ATPase α3 subunit ↓	0.01	0.08	Ca$_v$1.2 ↑	0.08	0.20
			Ca$_v$3.2 ↓	0.07	0.17
			Ca$_v$α2δ2 ↓	0.02	0.08
			CLC-3 ↑	<0.01	0.02
			K$_v$4.2 ↓	0.06	0.16
			K$_v$4.3 ↓	0.01	0.06
			KChIP2 ↓	0.02	0.08
			K$_v$2.1 ↓	0.05	0.15
			ERG1 ↓	0.07	0.18
			K$_{ir}$2.2 ↓	0.08	0.19
			K$_{ir}$2.4 ↓	<0.01	0.04
			K$_{ir}$3.1 ↓	<0.01	0.02
			K$_{ir}$3.4 ↓	0.02	0.08
			K$_{ir}$6.2 ↓	0.01	0.07
			SUR1 ↓	0.01	0.04
			TASK1 ↓	0.03	0.10
			Cx45 ↑	0.06	0.17
			Na$^+$/K$^+$ ATPase α1 subunit ↑	0.03	0.10
			Na$^+$/K$^+$ ATPase α2 subunit ↓	0.01	0.07
			Na$^+$/K$^+$ ATPase α3 subunit ↓	<0.01	0.01
			Na$^+$/K$^+$ ATPase β1 subunit ↓	0.04	0.11
			α1b adrenergic receptor ↓	0.01	0.05

Table S4. Summary of cell models used in 1D strand, strand dimensions and intercellular conductances.

Cell model	Number of cells	Length (mm)	Conductance (nS)
Atrium[17]	150	15.0	1000
Atrio-nodal[18]	50	5.0	500
Nodal[18]	25	2.5	290
Nodal-His[18]	50	5.0	500
Purkinje fibre[19]	200	20.0	3000
Left ventricle[19]	100	10.0	1150

Table S5. Single channel conductances used in calculations.

Channel	Single channel conductance
I_f	
HCN1	13.3 pS[35]
HCN4	16.9 pS[35]
I_{Na}	
Na$_v$1.1	17.0 pS[36]
Na$_v$1.5	17.3 pS[37]
$I_{Ca,L}$	
Ca$_v$1.2	19.0 pS[38]
Ca$_v$1.3	21.0 pS[38]
$I_{Ca,T}$	
Ca$_V$3.1	9.5 pS[39]
Ca$_V$3.2	7.2 pS[39]
I_{to}	
K$_v$1.4	4.0 pS[40]
K$_v$4.2	18.3 pS[41]
K$_v$4.3	4.0 pS[42]
$I_{K,1}$	
K$_{ir}$2.1	23.8 pS[43]
K$_{ir}$2.2	34.0 pS[43]
Electrical coupling	
Cx30.2	9.0 pS[44]
Cx40	200.0 pS[44]
Cx43	80.0 pS[44]
Cx45	30.0 pS[44]

Table S6. Calculation of ionic conductances in PHT in atrial muscle.

Atrium					
Current	**Protein**	**Control (×10^{-4})**	**Pulmonary hypertension (×10-4)**	γ_{ion} (pS)	**Scaling factor for conductance (percentage)**
I$_{Na}$	Na$_V$1.1	351	214	17.0	162
	Na$_V$1.5	4650	7881	17.3	
I$_{Ca,L}$	Ca$_V$1.2	309	141	19.0	46
	Ca$_V$1.3	3	0	21.0	
I$_{to}$	K$_v$1.4	254	91	4.0	36
	K$_v$4.2	49	7	18.3	
	K$_v$4.3	1192	583	4.0	
I$_{K,ur}$ or I$_{sus}$ or I$_{K,p}$	K$_v$1.5	533	393	-	74
I$_{K,r}$	ERG1	201	78	-	39
I$_{K,s}$	K$_V$LQT1	691	573	-	83
I$_{K,1}$	K$_{ir}$2.1	475	227	23.8	38
	K$_{ir}$2.2	611	203	34.0	
I$_{NaCa}$	NCX1	5853	4257	-	73
I$_{Ca,p}$	PMCA1	488	504	-	103
I$_{NaK}$ or I$_p$	α1 Na$^+$-K$^+$ pump	16412	11570	-	68
	α2 Na$^+$-K$^+$ pump	1912	758	-	
	α3 Na$^+$-K$^+$ pump	99	128	-	
Electrical coupling	Cx30.2	0	0	9.0	59
	Cx40	159	269	200.0	
	Cx43	5780	2866	80.0	
	Cx45	812	806	30.0	

Table S7. Calculation of ionic conductances in PHT in transitional tissue.

Transitional tissue (AN cell)					
Current	**Protein**	**Control ($\times 10^{-4}$)**	**Pulmonary hypertension (×10-4)**	γ_{ion} (pS)	**Scaling factor for conductance (percentage)**
I_{Na}	$Na_V1.1$	317	139	17.0	151
	$Na_V1.5$	2087	3475	17.3	
$I_{Ca,L}$	$Ca_V1.2$	451	259	19.0	57
	$Ca_V1.3$	0	0	21.0	
$I_{to,slow}$	$K_v1.4$	90	27	-	30
$I_{to,fast}$	$K_v4.2$	7	0	18.3	62
	$K_v4.3$	728	468	4.0	
$I_{K,r}$	ERG1	76	17	-	22
$I_{K,1}$	$K_{ir}2.1$	359	196	23.8	42
	$K_{ir}2.2$	114	16	34.0	
J_{rel}	RyR2	4239	596	-	16
	RyR3	66	72	-	
J_{up}	SERCA2a	140658	77857	-	55
I_{NaCa}	NCX1	2094	1026	-	49
I_{NaK} or I_p	α1 Na^+-K^+ pump	18654	15430	-	81
	α2 Na^+-K^+ pump	1729	1064	-	
	α3 Na^+-K^+ pump	182	98	-	
Electrical coupling	Cx30.2	1	0	9.0	65
	Cx40	987	791	200.0	
	Cx43	6653	3830	80.0	
	Cx45	1017	920	30.0	

Table S8. Calculation of ionic conductances in PHT in the compact node.

Compact node (N cell)					
Current	**Protein**	**Control (×10^{-4})**	**Pulmonary hypertension (×10-4)**	γ_{ion} (pS)	**Scaling factor for conductance (percentage)**
I_f	HCN1	411	359	13.3	31
	HCN2	12	15	35	
	HCN4	11775	3474	16.9	
$I_{Ca,L}$	Ca$_V$1.2	246	112	19.0	46
	Ca$_V$1.3	1	0	21.0	
$I_{to,slow}$	K$_v$1.4	29	25	-	84
$I_{to,fast}$	K$_v$4.2	0	0	18.3	67
	K$_v$4.3	451	299	4.0	
$I_{K,r}$	ERG1	25	26	-	102
J_{rel}	RyR2	4403	1670	-	38
	RyR3	24	28	-	
J_{up}	SERCA2a	70401	62299	-	88
I_{NaCa}	NCX1	2836	1996	-	70
I_{NaK} or I_p	α1 Na^+-K^+ pump	17540	13922	-	76
	α2 Na^+-K^+ pump	1546	1031	-	
	α3 Na^+-K^+ pump	1069	281	-	
Electrical coupling	Cx30.2	2	1	9.0	102
	Cx40	56	57	200.0	
	Cx43	154	247	80.0	
	Cx45	1284	1076	30.0	

Table S9. Calculation of ionic conductances in PHT in the penetrating bundle.

Penetrating Bundle (NH cell)					
Current	**Protein**	**Control ($\times10^{-4}$)**	**Pulmonary hypertension (×10-4)**	γ_{ion} (pS)	**Scaling factor for conductance (percentage)**
I_{Na}	$Na_V1.1$	70	79	17.0	169
	$Na_V1.5$	1546	2656	17.3	
$I_{Ca,L}$	$Ca_V1.2$	278	168	19.0	60
	$Ca_V1.3$	1	0	21.0	
$I_{to,slow}$	$K_v1.4$	22	18	-	84
$I_{to,fast}$	$K_v4.2$	0	4	18.3	51
	$K_v4.3$	369	170	4.0	
$I_{K,r}$	ERG1	29	28	-	96
$I_{K,1}$	$K_{ir}2.1$	352	380	23.8	111
	$K_{ir}2.2$	32	42	34.0	
J_{rel}	RyR2	1678	3005	-	180
	RyR3	12	28	-	
J_{up}	SERCA2a	24420	26945	-	110
I_{NaCa}	NCX1	3283	1313	-	40
I_{NaK} or I_p	α1 Na$^+$-K$^+$ pump	13448	15316	-	106
	α2 Na$^+$-K$^+$ pump	2169	1559	-	
	α3 Na$^+$-K$^+$ pump	402	97	-	
Electrical coupling	Cx30.2	1	0	9.0	88
	Cx40	988	535	200.0	
	Cx43	139	1022	80.0	
	Cx45	2530	2006	30.0	

Table S10. Calculation of ionic conductances in PHT in ventricular muscle.

Current	Protein	Control (×10^{-4})	Pulmonary hypertension (×10-4)	γ_{ion} (pS)	Scaling factor for conductance (percentage)
I_{Na}	$Na_V1.1$	187	272	17.0	63
	$Na_V1.5$	7765	4776	17.3	
$I_{Ca,L}$	$Ca_V1.2$	193	310	19.0	161
	$Ca_V1.3$	0	0	21.0	
$I_{Ca,T}$	$Ca_V3.1$	78	57	9.5	77
	$Ca_v3.2$	476	373	7.2	
$I_{to,slow}$	$K_v1.4$	63	65	-	103
$I_{to,fast}$	$K_v4.2$	47	19	18.3	40
	$K_v4.3$	444	182	4.0	
$I_{K,ur}$ or I_{sus} or $I_{K,p}$	$K_v1.5$	301	254	-	84
$I_{K,r}$	ERG1	109	64	-	59
$I_{K,s}$	K_VLQT1	753	579	-	77
$I_{K,1}$	$K_{ir}2.1$	708	753	23.8	87
	$K_{ir}2.2$	262	132	34.0	
J_{rel}	RyR2	18797	13525	-	72
	RyR3	56	64	-	
J_{up}	SERCA2a	61344	164649		268
I_{NaCa}	NCX1	3811	3025	-	79
$I_{Ca,p}$	PMCA1	444	338	-	76
I_{NaK} or I_p	$\alpha1$ Na^+-K^+ pump	5604	8289	-	112
	$\alpha2$ Na^+-K^+ pump	3326	1942	-	
	$\alpha3$ Na^+-K^+ pump	208	34	-	
Electrical coupling	Cx30.2	0	0	9.0	80
	Cx40	298	456	200.0	
	Cx43	4978	3214	80.0	
	Cx45	449	900	30.0	

Table S11. Summary of remodelling of ionic currents in PHT in different cell types. I_f, funny current; I_{Na}, Na^+ current; $I_{Ca,L}$, L-type Ca^{2+} current; $I_{Ca,T}$, T-type Ca^{2+} current; I_{to}, transient outward K^+ current; $I_{to,slow}$, slow component of I_{to}; $I_{to,fast}$, fast component of I_{to}; $I_{K,ur}$ (or I_{sus} or $I_{K,p}$), ultra-rapid delayed rectifier K^+ current; $I_{K,r}$, rapid delayed rectifier K^+ current; $I_{K,s}$, slow delayed rectifier K^+ current; $I_{K,1}$, background inward rectifier K^+ current; J_{rel}, sarcoplasmic reticulum Ca^{2+} release; J_{up}, sarcoplasmic reticulum Ca^{2+} uptake; I_{NaCa}, Na^+-Ca^{2+} exchange current; $I_{Ca,p}$ (or I_{SLCap}), sarcolemmal Ca^{2+} pump current; I_{NaK} (or I_p), Na^+-K^+ pump current.

Current	**Atrial muscle**	**Atrio-nodal (AN) cells**	**Nodal (N) cells**	**Nodal-His (NH) cells**	**Purkinje fibres & ventricle**
I_f	-	-	31%	-	-
I_{Na}	162%	151%	-	169%	63%
$I_{Ca,L}$	46%	57%	46%	60%	161%
$I_{Ca,T}$	-	-	-	-	77%
I_{to}	36%	-	-	-	-
$I_{to,slow}$	-	30%	84%	84%	103%
$I_{to,fast}$	-	62%	67%	51%	40%
$I_{K,ur}$ or I_{sus} or $I_{K,p}$	74%	-	-	-	84%
$I_{K,r}$	39%	22%	102%	96%	59%
$I_{K,s}$	83%	-	-	-	77%
$I_{K,1}$	38%	42%	-	111%	87%
J_{rel}	-	16%	38%	180%	72%
J_{up}	-	55%	88%	110%	268%
I_{NaCa}	73%	49%	70%	40%	79%
$I_{Ca,p}$ or I_{SLCap}	103%	-	-	-	76%
I_{NaK} or I_p	68%	81%	76%	106%	112%
Electrical coupling	59%	65%	102%	88%	80

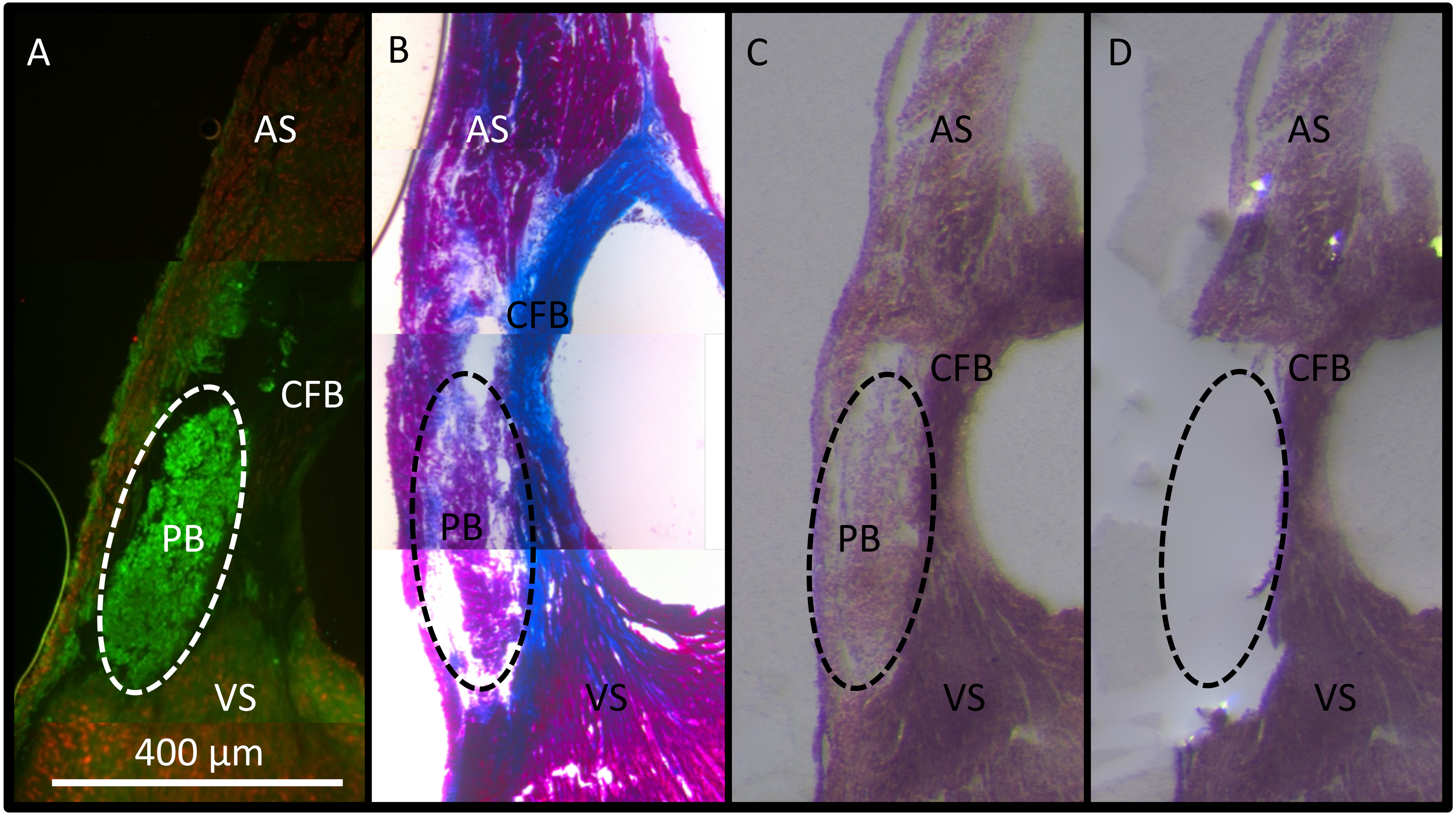

Fig. S1. Images demonstrating hand microdissection of the AV node. A, AV node section double immunolabelled for HCN4 (green) and Cx43 (red). The ringed area shows high levels of HCN4 and low levels of Cx43 and corresponds to the penetrating bundle (PB). B, Masson's trichrome staining of a 'sister section'. The area of interest demonstrated in panel A can be seen to be bordered by the central fibrous body (stained bright blue). The combination of high levels of HCN4, low levels of Cx43 and the presence of the central fibrous body identifies this area as the penetrating bundle (PB). C, haematoxylin and eosin stained section before microdissection. This reveals the area of interest identified from the 'map' created by the images in panels A and B. D, the same slide as C post-microdissection with the area of interest (in this case the penetrating bundle) removed. AS, atrial septum; CFB, central fibrous body; VS, ventricular septum.

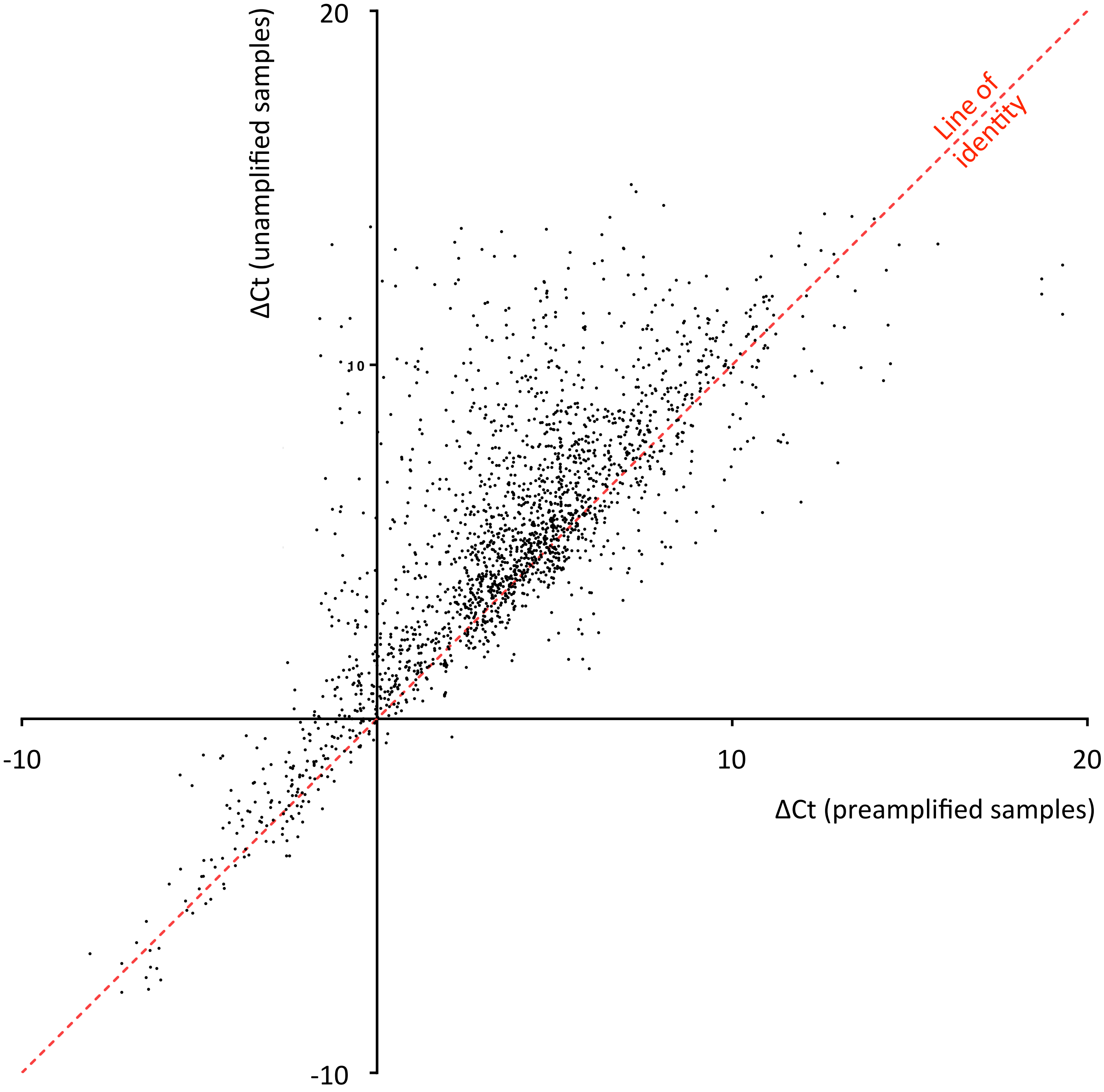

Fig. S2. Correlation of mRNA abundance (relative to that of the housekeeper; ΔCT) in unamplified and preamplified samples from the atrium and ventricle. See text for details. Linear regression analysis showed a significant correlation between the two ($R^2 = 0.62$; *P*<0001).

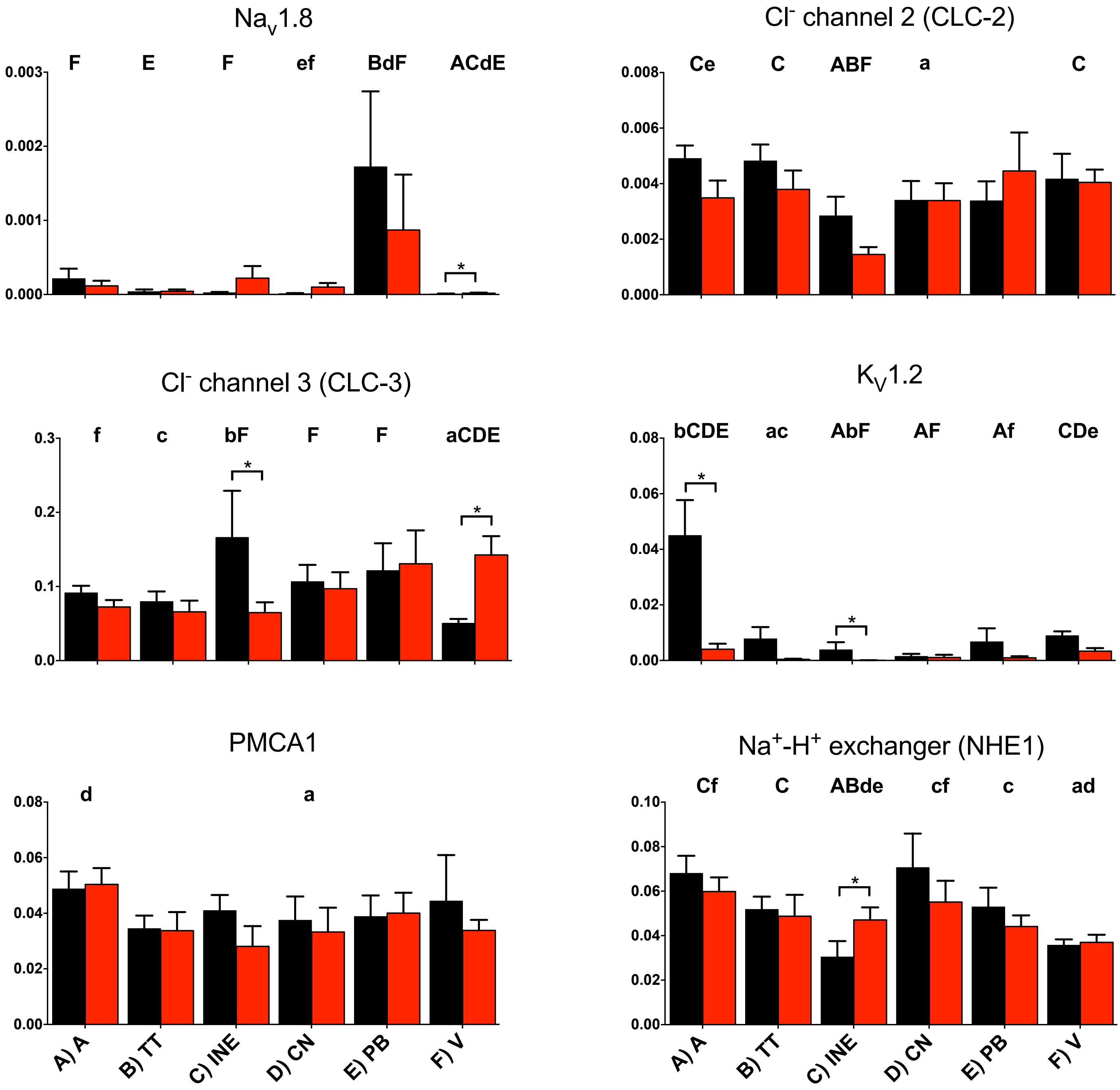

Fig. S3. Expression of miscellaneous transcripts in atrial muscle (A; A), transitional tissue (B; TT), inferior nodal extension (C; INE), compact node (D; CN), penetrating bundle (E; PB) and ventricular muscle (F; V) from control (black bars) and PHT (PHT; red bars) rats. In this and similar figures, means (+SEM) shown (n=6-8) and bars and asterisks indicate significant differences between the control and PHT rats assessed by the limma test (FDR-corrected *P*<0.2, i.e. 20%); for the control tissues only, letters indicate a significant difference from the appropriately lettered region (lower case letters, FDR-corrected *P*<0.2, i.e. 20%; upper case letters, FDR-corrected *P*<0.05, i.e. 5%).

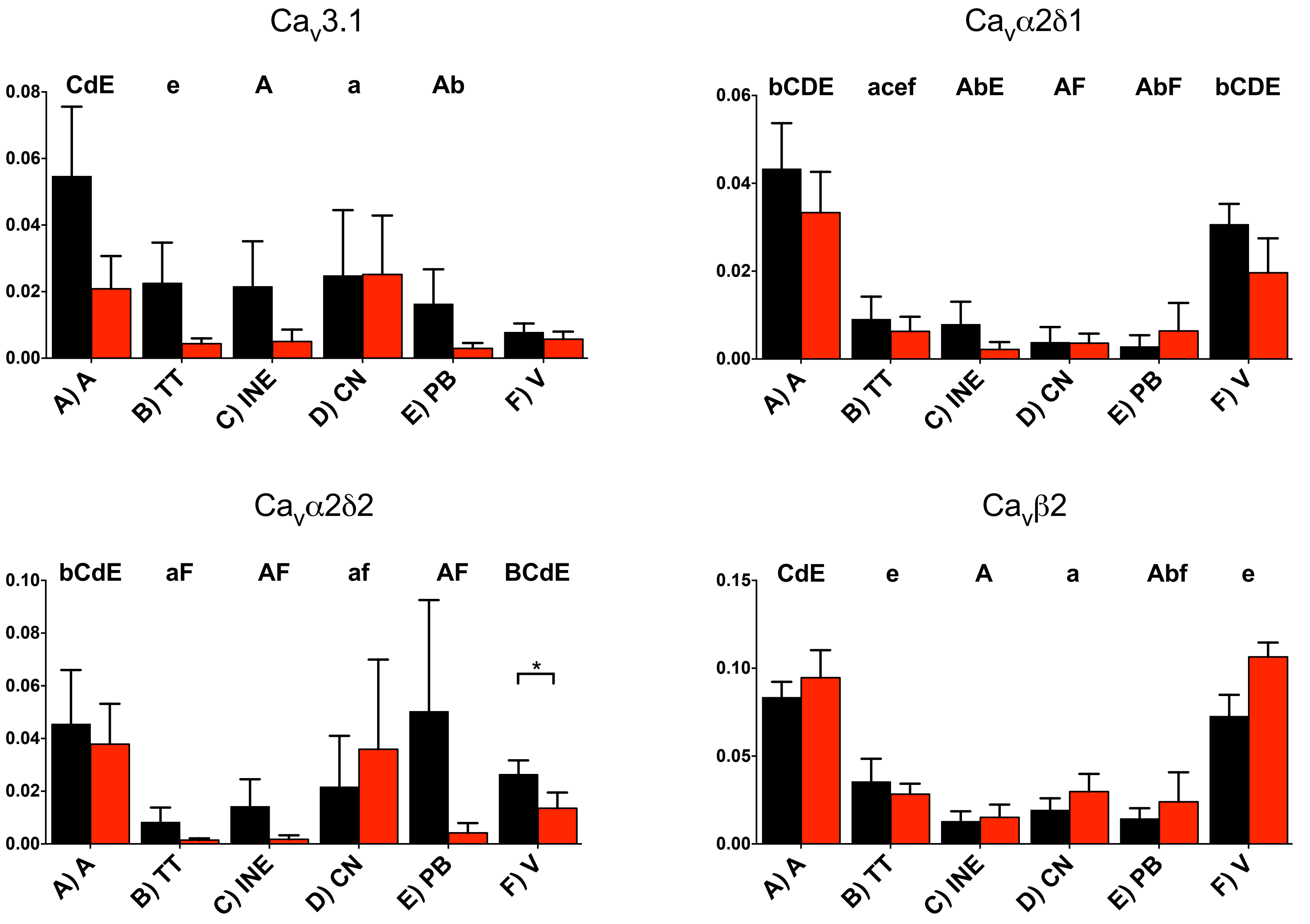

Fig. S4. **Expression at the mRNA level of Ca^{2+} channel subunits in atrial muscle (A; A), transitional tissue (B; TT), inferior nodal extension (C; INE), compact node (D; CN), penetrating bundle (E; PB) and ventricular muscle (F; V) from control (black bars) and PHT (red bars) rats.**

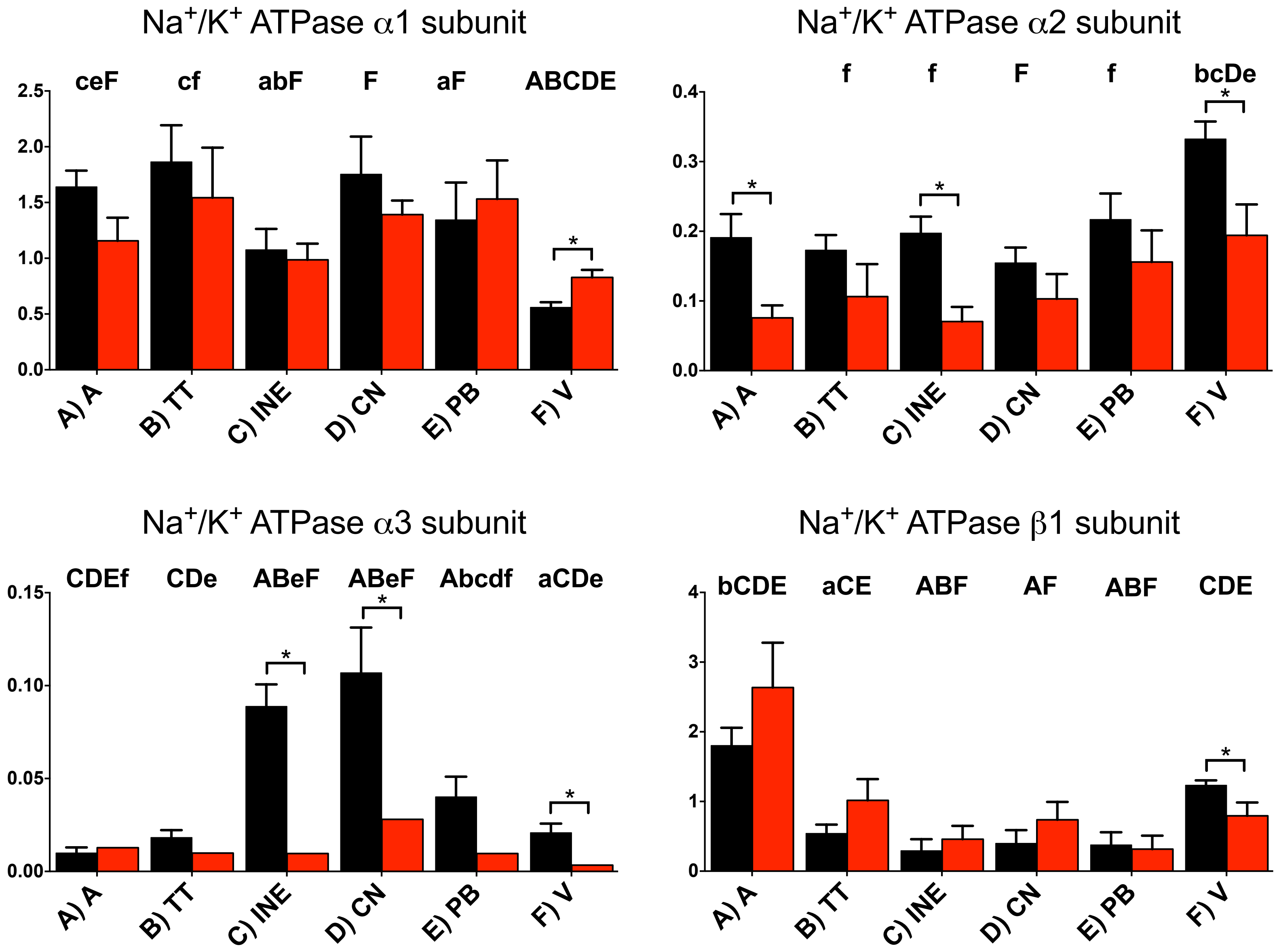

Fig. S5. Expression at the mRNA level of Na^+-K^+ pump subunits in atrial muscle (A; A), transitional tissue (B; TT), inferior nodal extension (C; INE), compact node (D; CN), penetrating bundle (E; PB) and ventricular muscle (F; V) from control (black bars) and PHT (red bars) rats.

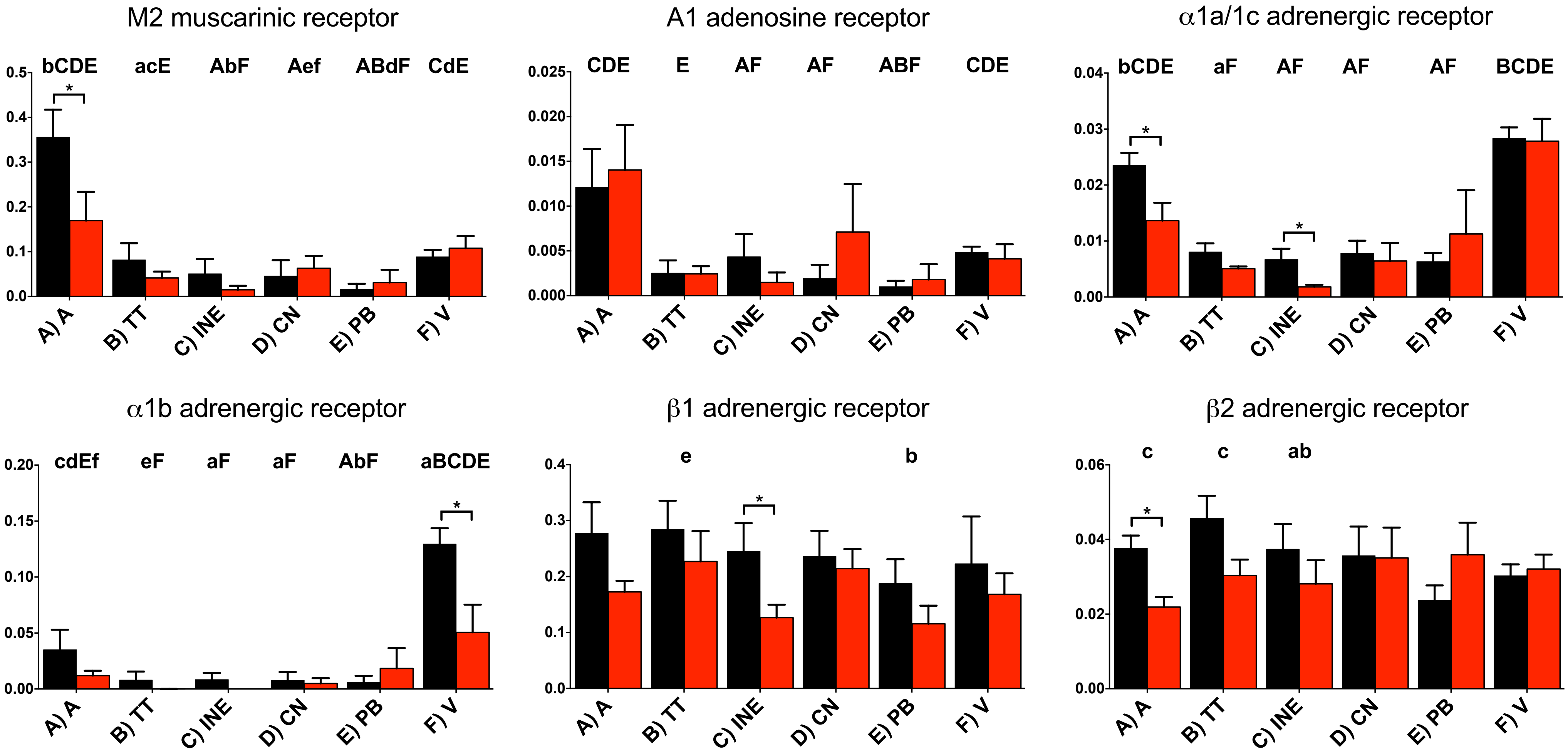

Fig. S6. Expression at the mRNA level of receptors in atrial muscle (A; A), transitional tissue (B; TT), inferior nodal extension (C; INE), compact node (D; CN), penetrating bundle (E; PB) and ventricular muscle (F; V) from control (black bars) and PHT (red bars) rats.

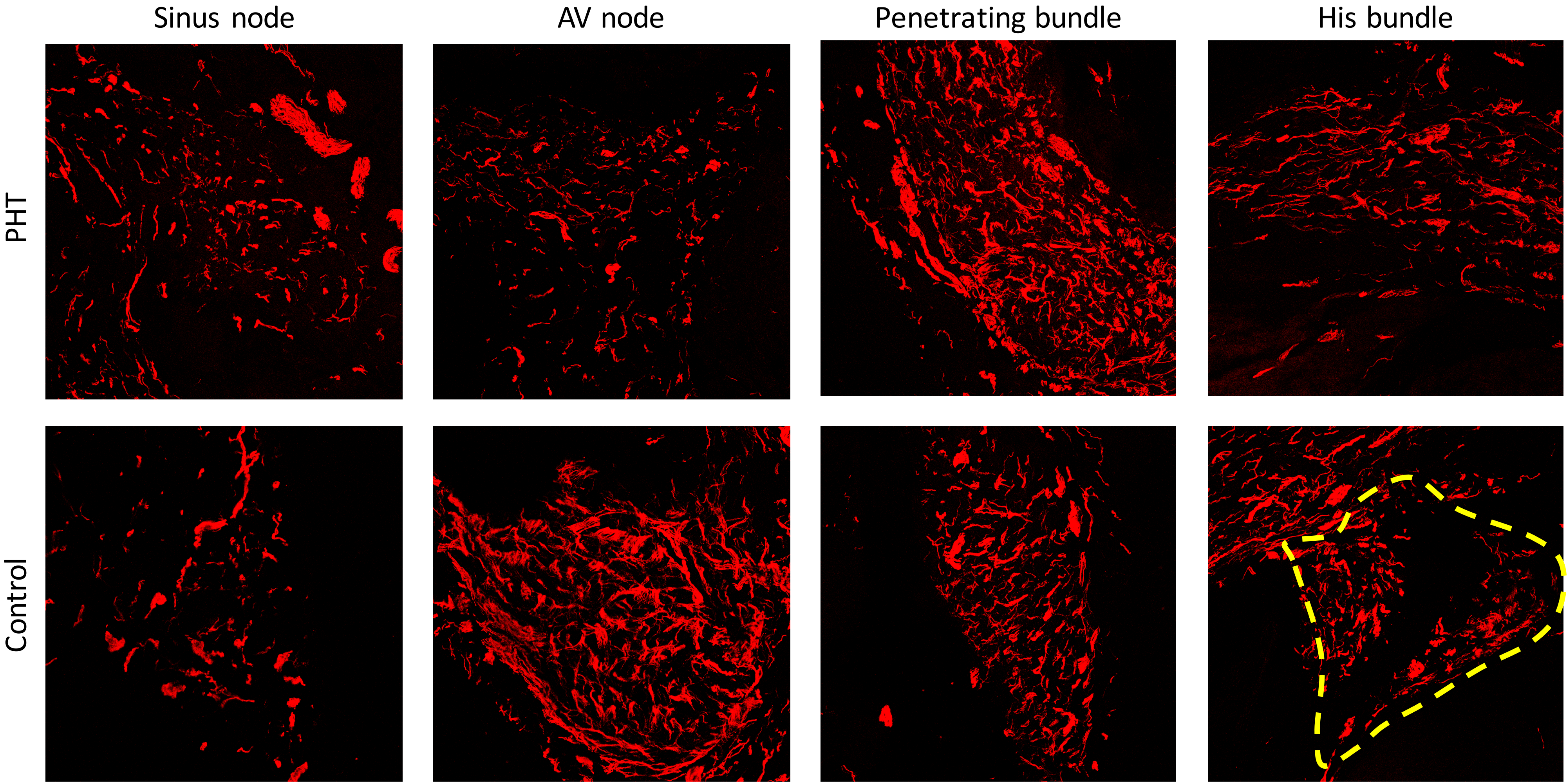

Fig. S7. Immunohistochemical labelling of neurofilament 150 (red signal; sympathetic neurone marker) in four parts of the cardiac conduction system including the AV node in control and PHT rats. The His bundle in the control rat is outlined in yellow.

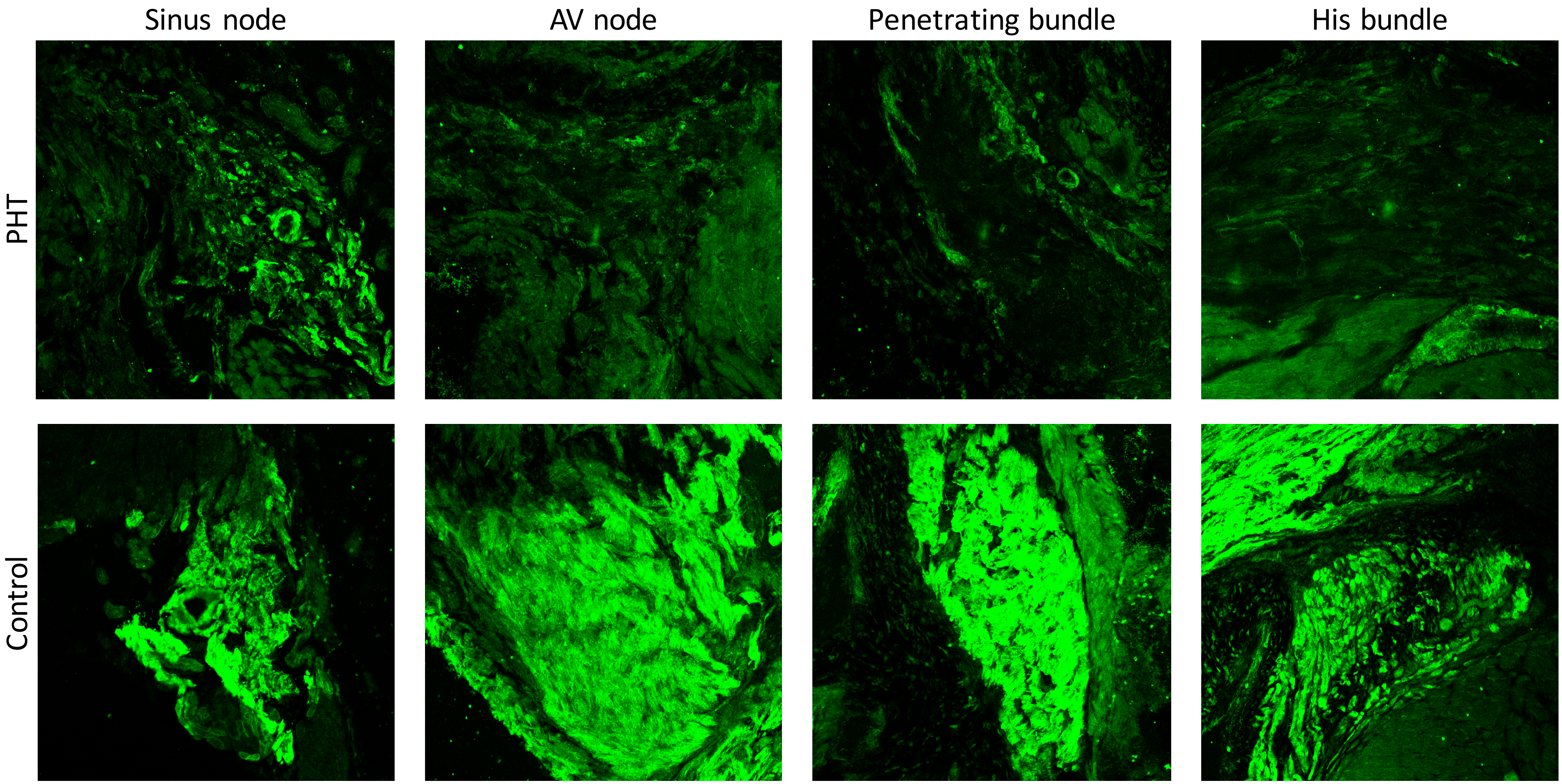

Fig. S8. Immunohistochemical labelling of HCN4 (green signal) in four parts of the cardiac conduction system including the AV node in control and PHT rats.